INORGANIC CHEMISTRY
FRONTIERS

RESEARCH ARTICLE

View Article Online
View Journal | View Issue

Cite this: *Inorg. Chem. Front.*, 2022, **9**, 2952

Facile and efficient photocatalyst for degradation of chlortetracycline promoted by H_2O_2†

Yuting Bai, [a] Meirong Han, [a] Xiangrui Li,[a] Sisi Feng, *[a,b] Liping Lu *[a] and Shengqian Ma *[c]

The composite photocatalyst based on a cerium(III) metal–organic framework (**MOF-1** or **1**), graphene oxide (GO), and Fe_3O_4 was constructed for the first time and was investigated for the degradation of chlortetracycline. A superior synergistic effect of graphene oxide and **MOF-1** was achieved for improving photocatalysis. The optimal composite (**1**/GO/Fe_3O_4) with 9.0 wt% graphene oxide displayed the highest photocatalytic performance in the degradation of chlortetracycline with the help of hydrogen peroxide (H_2O_2), with a removal rate of 80.5% in 180 minutes, which exhibited much higher photocatalytic performance than that of parent **MOF-1**. The enhanced photocatalytic performance was mainly attributed to the modification of graphene oxide, which can inhibit the recombination of the photogenerated carrier as an electron transporter and improve the absorption of visible light. Furthermore, the composite displayed superparamagnetic behavior that permitted the magnetic separation and convenient recovery of the photocatalyst from the reaction mixture. Importantly, the photocatalyst exhibited high stability and could be used recurrently. The photocatalytic mechanism involved the excitation of electrons from the VB to the CB in **MOF-1** excited by visible light irradiation, the transport of electrons between **MOF-1** and graphene oxide, and the generation of active groups ($^{\bullet}OH$ and $^{\bullet}O_2^-$).

Received 25th February 2022,
Accepted 23rd April 2022

DOI: 10.1039/d2qi00412g

rsc.li/frontiers-inorganic

Introduction

With the rapid development of the pharmaceutical industry, antibiotics as a good kind of antimicrobial agent have been widely used in agricultural, animal husbandry, marine industry aquaculture, medical, and many other industries.[1–3] The widespread abuse of antibiotics has caused harmful antibiotic residues to be released into the natural ecological environment. Even though antibiotics are usually present in water at low concentrations, their existence and persistence threaten the aquatic and terrestrial life, and their effects cannot be ignored.[4] Moreover, antibiotics are difficult to decompose by common physicochemical methods and bio-treatment because of their high chemical stability, which poses a serious threat to the health of most organisms.[5–9] At present, antibiotic pollutants have been listed as pollutants that need priority treatment. Chlortetracycline, as a broad-spectrum drug with antibacterial activity, is one of the most common tetracycline antibiotics in livestock.[10] The residual chlortetracycline is difficult to degrade naturally in the natural environment, which can inhibit or destroy the growth of microorganisms due to the specificity of antibiotics to microorganisms.[11] Developing facile, efficient, and environmentally friendly treatment technologies to convert these pollutants into non-toxic or low-toxic substances is desperately needed. It is generally accepted that photocatalytic technology has undoubtedly become the first choice to solve environmental and energy issues because it is inexhaustible, low-priced, non-toxic, and harmless.

Photocatalysis is an advanced oxidation process, which has shown promising performance in wastewater treatment. Organic pollutants can be effectively decomposed or degraded by active groups (*e.g.* $^{\bullet}OH$, $^{\bullet}O_2^-$), which are produced by photocatalysts under UV-light, visible light or the sunlight. Many reports have proved that H_2O_2 can boost the photocatalytic performance of catalysts by capturing photogenerated electrons to generate $^{\bullet}OH$.[12] Recently, metal–organic frameworks (MOFs) have received great interest as novel environmental remediation materials for photocatalytic applications. Compared with conventional photocatalysts, most MOFs can use solar energy more efficiently because they can be modulated by the pore size of active sites to achieve the design and manufacture of the photocatalysts at the molecular level, and allow the good

[a]*Institute of Molecular Science, Key Laboratory of Chemical Biology and Molecular Engineering of the Education Ministry, Shanxi University, Taiyuan, Shanxi 030006, P. R. China. E-mail: ssfeng@sxu.edu.cn, luliping@sxu.edu.cn*
[b]*Key Laboratory of Materials for Energy Conversion and Storage of Shanxi Province, Shanxi University, Taiyuan, Shanxi, 030006, P. R. China*
[c]*Department of Chemistry, University of North Texas CHEM 305D, 1508 W Mulberry St, Denton, TX, 76201, USA. E-mail: Shengqian.Ma@unt.edu*

†Electronic supplementary information (ESI) available: Crystal details, PXRD, FT-IR, TGA and LC-MS. CCDC 2094467. For ESI and crystallographic data in CIF or other electronic format see DOI: https://doi.org/10.1039/d2qi00412g

accommodation and rapid transport of guest molecules.[13–15] These characteristics make MOFs photoresponsive catalysts, which can be induced to produce and transfer electrons between the interface of MOFs and H_2O_2 by light irradiation.

MOFs have been successfully used as a photocatalyst to degrade organic pollutants in wastewater. However, the dissatisfactory performance of pure MOFs, derived from the high recombination rate of photogenerated carriers, still needs to be improved. Further efforts have been devoted to improving the photocatalytic efficiency of MOFs. Currently, incorporating graphene oxide into MOFs has also been demonstrated to be a facile and effective strategy to achieve high photocatalytic activity.[16] This may be attributed to the following three reasons: (1) abundant functional groups on the surface of graphene oxide can help to fasten the metal cations of MOFs and facilitate the growth of MOFs on its surface, without destruction of the coordination structure of MOFs;[17–19] (2) excellent conductivity of the graphene oxide[20] help to reduce electron/hole recombination efficiency, and improve the photocatalytic performance of MOFs simultaneously;[21] (3) the large specific surface area of graphene oxide can be used as the carrier for MOF units, which plays a vital role in preventing the agglomeration of MOF particles in the layer and increasing the reactive sites. MOFs/GO composite materials combine the favorable properties of MOFs and graphene oxide. Recent attempts to fabricate MOF/graphene-based materials have achieved encouraging results.[22,23] Yang *et al.*[24] prepared a MIL-68(In)-NH_2/GrO composite to degrade amoxicillin, resulting in higher removal efficiency of amoxicillin (~93% at 120 min) than pure MIL-68(In)-NH_2. Fakhri and co-workers[25] synthesized a Zr-MOF@WO_3/graphene oxide photocatalyst that showed highly enhanced photodegradation of tetracycline. These results demonstrate that MOF/graphene-based materials are a potential new class of photocatalysts for the photocatalytic degradation of antibiotics. To the best of our knowledge, there has been no research on the degradation of chlortetracycline by MOFs. The composite photocatalyst discussed in this paper is the first study on the degradation of chlortetracycline by a material built on MOFs. Although there are some reports on the hybrid photocatalysts of MOF/GO, recycling from water is rarely achieved. Compositing super-paramagnetic Fe_3O_4 with the MOF/GO is an easy and efficient strategy[26] that permitted the magnetic separation and convenient recovery of photocatalysts from the reaction mixture.[27,28]

Inspired by the above, in this work, we chose $[Ce_2(TCPB)_2(DMF)(H_2O)]_n$ (**MOF-1** or **1**) composed of a 1,3,5-tris(4-carboxyphenoxy)benzene (H_3tcpb) ligand as the functional material. A novel three-component **1**/GO/Fe_3O_4 composite photocatalyst was prepared by incorporating graphene oxide and Fe_3O_4 into **MOF-1** for the sake of achieving boosting photocatalysis. Chlortetracycline was chosen as the target pollutant to evaluate the photocatalytic ability. The structure, physical properties, and photocatalytic activity of **1**/GO/Fe_3O_4 composite catalysts were compared with those of pure **MOF-1**. The degradation of chlortetracycline was optimized under various experimental conditions such as graphene oxide content, catalyst concentration, and H_2O_2 concentration. The feasible photocatalytic mechanism of chlortetracycline degradation was also proposed. The results of this work show that this novel composite photocatalyst can open a new avenue for unsolved problems in environmental treatment.

Results and discussion

Crystal structure of $[Ce_2(tcpb)_2(DMF)(H_2O)]_n$ (MOF-1 or 1)

X-ray crystallographic analysis indicates that **MOF-1** crystallizes in a $P\bar{1}$ space group, consisting of a Ce^{3+} cation, an H_3tcpb ligand, a half coordinated H_2O, and a half coordinated DMF in an asymmetric unit (Fig. 1a). Each central Ce^{3+} cation coordinated with eight oxygen atoms from seven carboxylate groups of H_3tcpb ligands (O1, $O2^{ii}$, $O6^{i}$, $O7^{iv}$, $O7^{v}$, $O8^{iii}$, $O9^{iii}$), a half coordinated H_2O (O10), and a half coordinated DMF (O11), showing a distorted dodecahedron (Fig. 1b). The distances of the Ce–O bond range from 2.366 (4) to 2.687 (5) Å. The distances of the Ce–O_{DMF} bond (2.517 (9) Å) and the Ce–O_{water} bond (2.527 (10) Å) are longer than that of Ce–$O_{carboxyl}$ (2.366 (4) Å), suggesting the stronger interaction between the central Ce^{3+} cation and H_3tcpb ligand.

The carboxylate groups of $tcpb^{3-}$ anions link adjacent Ce^{3+} cations to develop a binuclear 1D chain with a Ce···Ce distance of 5.5405(5) (Fig. 1c), which is further connected by $tcpb^{3-}$ ligands forming a 2D layer (Fig. 1d). As shown in Fig. 1e, the 2D layers are alternately connected to a 3D supramolecular network *via* $tcpb^{3-}$ linkers. Topologically, the Ce^{3+} cation and $tcpb^{3-}$ ligand can be considered as two types of 6-connected nodes. Thus the structure of **MOF-1** can be simplified as a 6-connected network with a point symbol of $(4^{11}\cdot6^4)$ (Fig. 1f).

Characterization of MOF-1 and 1/GO/Fe_3O_4

As can be seen from Fig. S1,† the PXRD pattern of **MOF-1** is identical to the simulated one based on single crystal diffraction data, proving the phase purity of as-synthesized **MOF-1**. In Fig. S2,† the **MOF-1** exhibited a weight loss of approximately 6.8% in the range of 27.5–230 °C, which was assigned to the loss of coordinated H_2O and DMF molecules. The subsequent significant weight loss appeared at 530 °C corresponding to the decomposition of $tcpb^{3-}$ ligands within the framework, demonstrating that the main framework began to collapse from 530 °C. The thermal decomposition behavior of the **1**/GO/Fe_3O_4 composite was similar to that of **MOF-1**. Importantly, the composite displayed higher thermal stability compared to pure **MOF-1**, which may be attributed to the chemical bonding between the **MOF-1** and graphene oxide.

The ternary photocatalyst was characterized by PXRD, and the results are presented in Fig. 2a. After incorporating graphene oxide and Fe_3O_4, **1**/GO/Fe_3O_4 showed characteristic diffraction peaks of **MOF-1** and Fe_3O_4 but no obvious characteristic peaks of graphene oxide, which may be attributed to the small recombination ratio of graphene oxide (9%) and weak diffraction peak intensity of graphene oxide.[24] Similar phenomena have been reported in other research studies.[18]

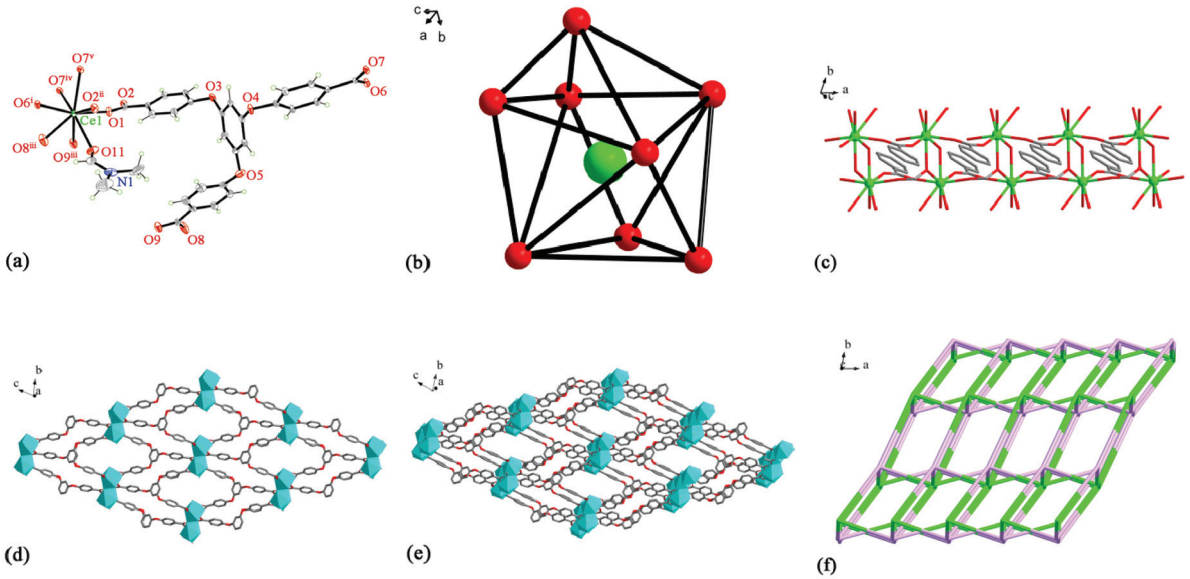

Fig. 1 (a) Coordination environment of the Ce^{3+} cation and the atomic labeling scheme in **MOF-1** (coordinated H_2O molecules are omitted for clarity). Symmetry codes: (i) *x*, *y*, *z* + 1; (ii) *x* + 1, *y*, *z*; (iii) −*x* + 1, −*y* + 1, −*z* + 2; (iv) *x* − 1, *y*, *z* + 1; and (v) −*x* + 2, −*y* + 2, −*z* + 1. (b) View of the distorted dodecahedron coordination of the Ce^{3+} cation in **MOF-1**. (c) 1D metal chains connected by Ce^{3+} cations and $tcpb^{3-}$ anions (H atoms are omitted for clarity). (d) View of the 2D layer of the structure. (e) 3D structure of **MOF-1**. (f) Topological structure of **MOF-1**. The Ce^{3+} cation and the $tcpb^{3-}$ anions are presented in green and purple, respectively.

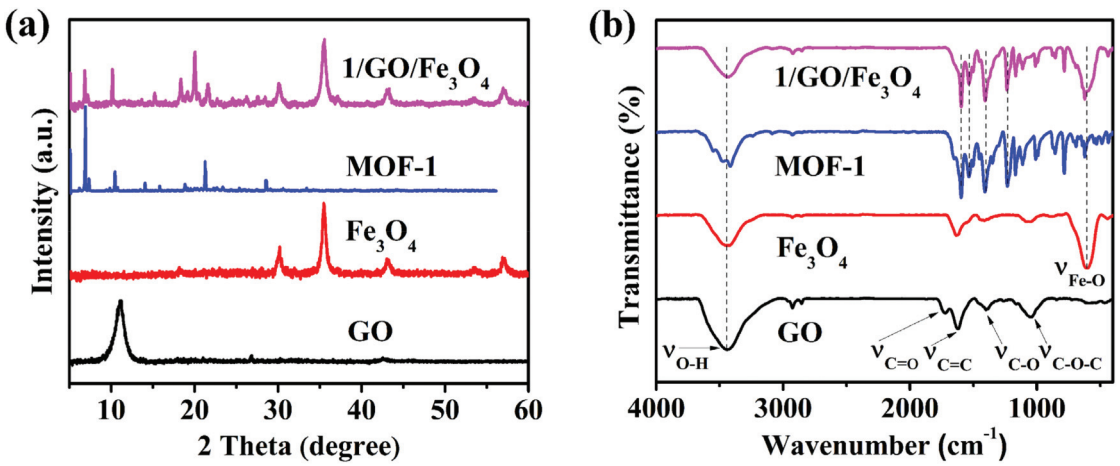

Fig. 2 PXRD patterns (a) and FT-IR spectra (b) of GO, Fe_3O_4, **MOF-1**, and **1**/GO/Fe_3O_4 (solid, temperature: 25 °C).

The PXRD results demonstrated the existence of **MOF-1** and Fe_3O_4 in the **1**/GO/Fe_3O_4 ternary photocatalyst.

The functional groups of the photocatalyst were identified by FT-IR (Fig. 2b). In graphene oxide, the characteristic absorption peaks at 3440, 1728, 1624, 1389, and 1107 cm^{-1} were assigned to the O–H, C=O, C=C, C–O, and C–O–C stretching vibrations, respectively, suggesting the existence of many oxygen-containing hydrophilic groups.[29] As for **MOF-1**, the peaks at 1600 and 1533 cm^{-1} were assigned to the C=C stretching vibrations; the peaks at 1400 and 1230 cm^{-1} corresponded to the C–H formation vibration and C–O–C stretching vibration. After incorporating Fe_3O_4, **1**/GO/Fe_3O_4 preserved the characteristic peaks of **MOF-1** and Fe_3O_4, demonstrating the successful synthesis of the ternary composite. Nevertheless, there are no obvious characteristic peaks of graphene oxide in the FT-IR spectra of the composites due to the high dispersion of graphene oxide.[30] Therefore, the results of FT-IR also only verified the incorporation of **MOF-1** and Fe_3O_4.

To further ascertain the existence of graphene oxide and Fe_3O_4, SEM was performed, which was favorable for understanding the surface morphologies and microstructures of the material. It can be seen from Fig. 3a and b that **MOF-1** was

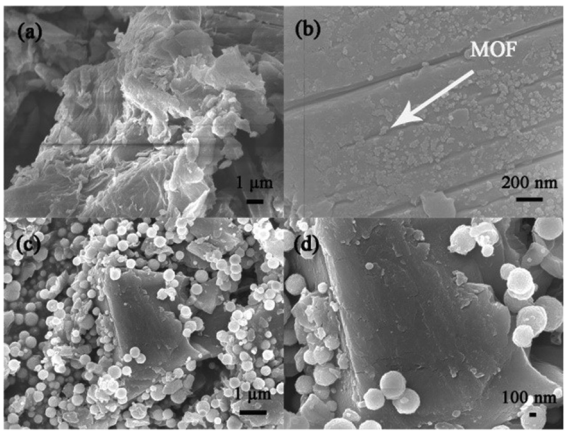

Fig. 3 SEM images of **MOF-1**/GO (a and b) and **1**/GO/Fe_3O_4 (c and d).

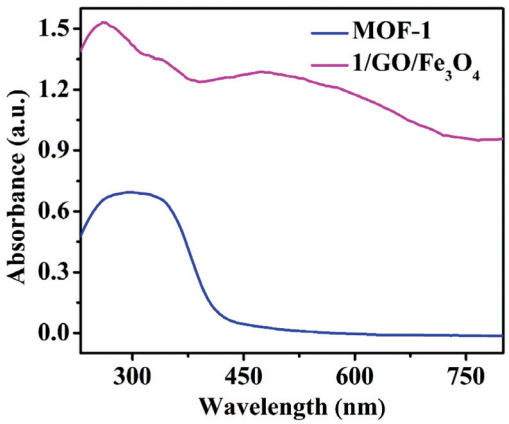

Fig. 4 UV–Vis diffuse reflectance spectra of **MOF-1** and the **1**/GO/Fe_3O_4 composite (solid, temperature: 25 °C).

successfully dispersed on graphene oxide. This phenomenon was consistent with our assumption that metal cations were well anchored on the surface of the graphene oxide sheets by oxygen-containing groups which acted as seed sites for the recombination of **MOF-1** and graphene oxide, reflecting strong interactions between **MOF-1** and graphene oxide. As shown in Fig. 3c and d, Fe_3O_4 nanoparticles with a uniform size of about 400 nm were dispersed on the surface of graphene oxide under ultrasonication, which was further confirmed by the fact that incorporation of Fe_3O_4 enabled the composite to be recovered under an external magnetic field (Fig. S5†). So the **1**/GO/Fe_3O_4 composite was distinctly formed.

The N_2 adsorption–desorption isotherms of **MOF-1** and **1**/GO/Fe_3O_4 were performed to figure out the specific surface area and Barrett–Joyner–Halenda (BJH) pore size. The porosity of **MOF-1** was too small to be considered, and the interaction between **MOF-1** and chlortetracycline was probably due to surface adsorption. After incorporating graphene oxide, the **1**/GO/Fe_3O_4 composite exhibited a larger specific area (16.35 $m^2 g^{-1}$) with the existence of mesoporous, and its isotherms belonged to the type IV curve with a narrow H3 hysteresis loop (Fig. S3†).[31] The results demonstrated that the addition of graphene oxide can boost the specific surface area of the composite.

The UV-vis diffuse reflectance spectra of **MOF-1** and **1**/GO/Fe_3O_4 were studied to evaluate the optical properties (Fig. 4). **MOF-1** exhibited broad absorption in the range of 230–400 nm. After incorporating graphene oxide, **1**/GO/Fe_3O_4 exhibited a new broad absorption in the visible region (400–800 nm), which may be attributed to the coupling between Ce^{3+} cations and oxygen-containing functional groups of graphene oxide, so it can be effectively excited by visible light.[32] Moreover, the color of the sample changed significantly (Fig. S4†). The pure **MOF-1** was primrose, while the **1**/GO and **1**/GO/Fe_3O_4 samples were uniform grey and brown, respectively, indicating the existence of graphene oxide. These results are in agreement with previous observations in other GO-based composites.[33]

Photocatalytic performance

The photocatalytic performance was further assessed by degrading chlortetracycline. As seen in Fig. 5a, without the photocatalyst, chlortetracycline showed excellent stability under visible light irradiation. When H_2O_2 was added to the chlortetracycline solution, the degradation efficiency increased a little under visible light. This may be ascribed to the photolysis of H_2O_2, which facilitated the formation of reactive $^{\bullet}OH$. **MOF-1** showed a certain catalytic degradation effect on chlortetracycline with a removal rate of 21.5% in 180 minutes, which can be improved to 26.8% in the presence of H_2O_2. This improved photocatalytic property can be attributed to the generation of $^{\bullet}OH$ and electron cycle at the catalytic site. On the one hand, H_2O_2 can capture photogenerated electrons in the excited **MOF-1** to generate $^{\bullet}OH$; on the other hand, Ce^{3+} on the **MOF-1** surface catalyzes the decomposition of H_2O_2 to produce $^{\bullet}OH$ ($Ce^{3+} + H_2O_2 \rightarrow Ce^{4+} + {}^{\bullet}OH + OH^-$, $Ce^{4+} + H_2O_2 \rightarrow Ce^{3+} + HO_2^{\bullet} + H^+$), achieving significantly enhanced photocatalytic performance.[12,33] However, the removal performance of chlortetracycline was still unsatisfactory owing to the poor separation and migration of photogenerated electron–hole pairs. Interestingly, compared to the single (**MOF-1**, graphene oxide) or binary (GO/Fe_3O_4) components, the **1**/GO/Fe_3O_4 composite exhibited obviously superior degradation efficiency to chlortetracycline, with a removal rate of 80.5% in 180 minutes under visible light. The outstanding degradation efficiency of the composite can be explained by the synergistic interplay between **MOF-1** and graphene oxide. Firstly, owing to the coupling between Ce^{3+} cations and oxygen-containing functional groups of graphene oxide, **MOF-1** can be excited by visible light in the **1**/GO/Fe_3O_4 composite to produce more electron and hole charge carriers, which facilitated the degradation of chlortetracycline. Secondly, photoinduced electrons can transfer quickly from the conduction band of **MOF-1** to the surface of graphene oxide, which reduced the recombination rate of the photogenerated carriers, and ultimately improved the photocatalytic performance of the composite. Moreover, similar degradation efficiency over **1**/GO and **1**/GO/Fe_3O_4 for

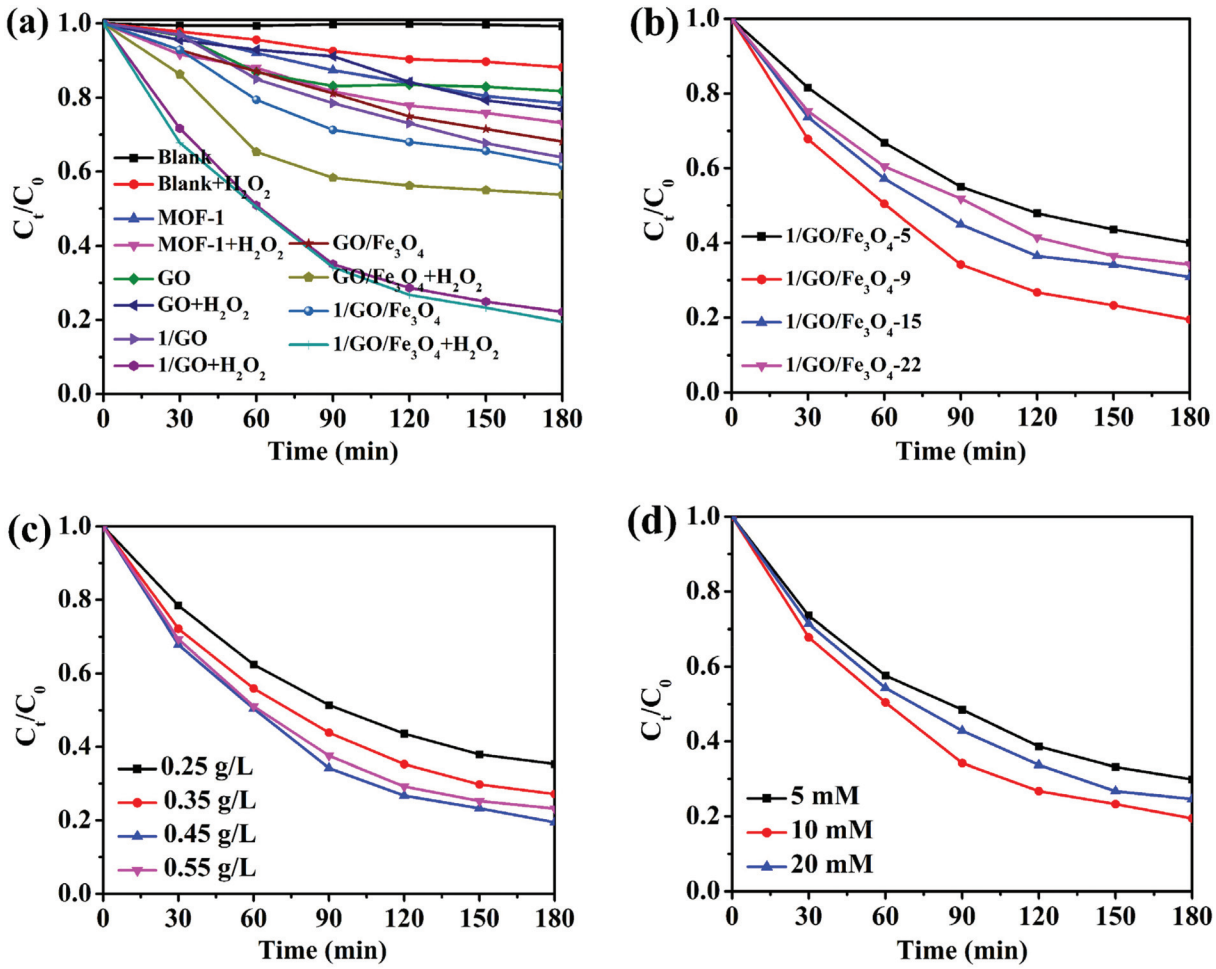

Fig. 5 (a) Photocatalytic degradation efficiency of chlortetracycline over different photocatalysts. Influence of the (b) GO content, (c) catalyst concentration, (d) H_2O_2 concentration on the degradation of chlortetracycline (except for the investigated parameter, other parameters were set as follows: 20 mg L^{-1} chlortetracycline, 0.45 g L^{-1} **1**/GO/Fe_3O_4, and 10 mM H_2O_2).

chlortetracycline indicated that the addition of Fe_3O_4 had no obvious degradation effect on the composite. Nevertheless, the incorporation of Fe_3O_4 endowed superparamagnetism to the composite, enabling the recycling of the composite through an external magnetic field (Fig. S5†).

The effect of graphene oxide amounts on photocatalytic efficiency was investigated and is displayed in Fig. 5b. When the loading graphene oxide amount changed from 5 wt% to 9 wt%, the degradation efficiency significantly increased from 59.9% to 80.5%. However, when the graphene oxide amount is further increased, its degradation efficiency began to decrease, which may be attributed to the shield of the active sites of **MOF-1** by excessive graphene oxide.[30,34] The results manifest that the optimum amount of graphene oxide is the key to improving the photocatalytic efficiency. The best degradation efficiency of **1**/GO/Fe_3O_4-9 was up to 80.5% under H_2O_2/Vis conditions, which may be ascribed to the increased active sites, large light absorption efficiency, and high electron–hole separation efficiency. By analyzing first-order kinetics plots of the catalysts, it can be seen that the degradation rate constants of **1**/GO/Fe_3O_4-5, **1**/GO/Fe_3O_4-9, **1**/GO/Fe_3O_4-15, and **1**/GO/Fe_3O_4-22 are 0.0052, 0.0092, 0.0066, and 0.0060 min^{-1}, respectively (Fig. S6†). The kinetic constants of **1**/GO/Fe_3O_4-9 were 1.8, 1.4, and 1.5 times higher than those of **1**/GO/Fe_3O_4-5, **1**/GO/Fe_3O_4-15, and **1**/GO/Fe_3O_4-22, respectively. Therefore, the optimal graphene oxide loading ratio in the **1**/GO/Fe_3O_4 composite is 9 wt%. Compared with similar studies shown in Table 1, it is clear that the catalyst in this work has a better comprehensive evaluation concerning the degradation efficiency and recyclability.

The effect of the composite catalyst dosage was tested and the results are presented in Fig. 5c. The degradation efficiency of chlortetracycline increased from 64.7% to 80.5% as the **1**/GO/Fe_3O_4 concentration changed from 0.25 to 0.45 g L^{-1}. It was probably because an appropriate increase of the catalyst concentration can provide more active sites for photocatalysis, leading to the promotion of chlortetracycline degradation. However, when the catalyst concentration further increased to 0.55 g L^{-1}, the declination of degradation efficiency was observed. It was owing to the excessive particles, catalyst aggre-

Table 1 Comparison of the photocatalytic performance of the **1**/GO/Fe_3O_4 composite with some reported photocatalysts in the degradation of chlortetracycline (CTC)

[PhotoCatalyst] (g L^{-1})	[Antibiotics] (mg L^{-1})	Light source	Degradation (%)	Ref.
JLUE-MOG-1 (1.0)	CTC (100)	Xenon lamp (300 W)	100.0 (40 minutes)	37
TiO_2 (1.0)	CTC (10)	UVA	95.5 (120 minutes)	38
BP-BVO (1.5)	CTC (10)	LED lamp (100 W)	88.0 (120 minutes)	39
1/GO/Fe_3O_4 (0.45)	CTC (20)	Xenon lamp (300 W)	80.5 (180 minutes)	This work
$SnFe_2O_4$ (1.0)	CTC (50)	Iodine tungsten lamp (300 W)	75.0 (150 minutes)	40
Cu_3P-$ZnSnO_3$-g-C_3N_4 (1.0)	CTC (10)	Xenon lamp (500 W)	63.5 (60 minutes)	41
TiO_2-NS/Pt/GO (0.2)	CTC (50)	Xenon lamp (500 W)	45.0 (90 minutes)	42

gation, turbidity increment and light scattering that occurred in the reaction solution, which resulted in the inhibition of photon penetration, the reduction of active sites, and thus the decrease of the degradation efficiency. So the optimum composite catalyst concentration was 0.45 g L^{-1}.[35]

Since H_2O_2 can obviously enhance the photocatalyst activity, the effect of H_2O_2 concentration was also studied. As presented in Fig. 5d, different H_2O_2 concentrations (from 5 to 20 mM) were investigated. It was apparent that the degradation efficiency of chlortetracycline in 180 minutes increased from 70.1 to 80.5% with an increase in the H_2O_2 concentration from 5 to 10 mM. Because more $^{\bullet}OH$ radicals can be generated to degrade chlortetracycline. However, a further increase of the H_2O_2 concentration to 20 mM would result in a decrease of chlortetracycline degradation (75.3%), which may be attributed to the scavenging effect of excessive H_2O_2 to $^{\bullet}OH$ radicals. Accordingly, an optimum H_2O_2 concentration of 10 mM could be found.[36]

In practical applications, it is crucial to study the stability of the photocatalyst during the photocatalytic process. To evaluate the stability and reusability of **1**/GO/Fe_3O_4, photodegradation of chlortetracycline was carried out repeatedly under visible light. The photocatalyst was recycled by an applied magnetic field and washed with distilled water for the next cycle. As shown in Fig. 6a, there was no evident loss of photocatalytic performance for chlortetracycline degradation over **1**/GO/Fe_3O_4 after six cycles, which supported that **1**/GO/Fe_3O_4 possessed excellent stability in photocatalytic performance. Furthermore, the PXRD and FT-IR of **1**/GO/Fe_3O_4 before and after the chlortetracycline degradation were performed and the results are shown in Fig. S7a and b.† The PXRD patterns and FT-IR spectra of composites were identical to the fresh ones, proving outstanding stability.[43] The pH of the solution is another key factor that can remarkably affect photocatalysis. The effect of initial pH on the degradation efficiency of chlortetracycline using **1**/GO/Fe_3O_4 was determined. As shown in Fig. 6b, **1**/GO/Fe_3O_4 exhibited relatively good and stable catalytic performance in the pH range of 3.0 to 7.0. When the pH increased to 8.0, the photodegradation process was hindered significantly, which may be attributed to that acidic conditions were more conducive to the production of $^{\bullet}OH$. However, an extreme acid solution may result in poor performance in photodegradation processes. This result demonstrates that **1**/GO/Fe_3O_4 can work effectively in a wide range of pH. Based on the above results, the **1**/GO/Fe_3O_4 composite can be expected as a promising candidate for organic pollutant removal in practical applications because of its excellent photocatalytic performance and outstanding chemical stability.

There are some co-existing species in actual wastewater, such as inorganic salts and even organics, which may affect the degradation efficiency of the photocatalyst.[44] To evaluate the practical application potential, the photocatalytic perform-

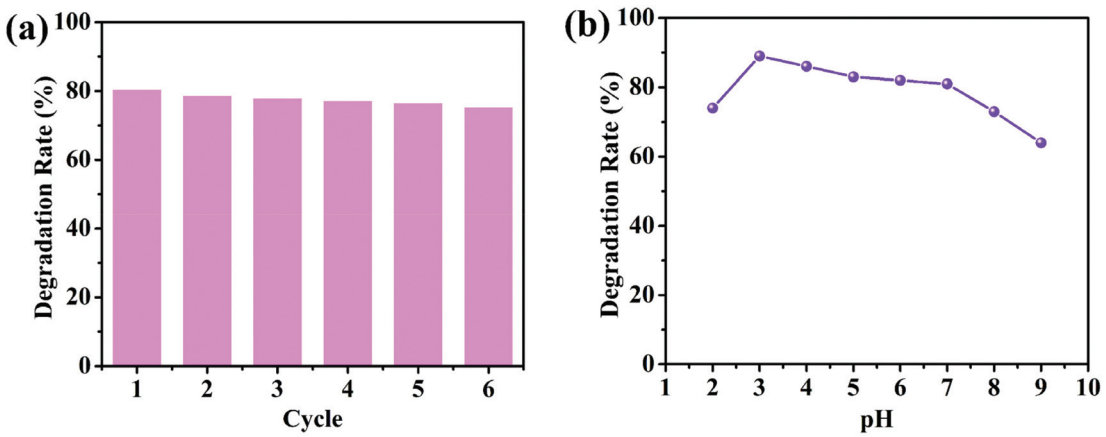

Fig. 6 (a) Recycling tests for the degradation of chlortetracycline by the **1**/GO/Fe_3O_4-9 composite. (b) Effects of the initial pH on the degradation of chlortetracycline.

ance of the composite was explored in simulated wastewater samples including chlortetracycline with known concentrations in real tap water and river water, respectively. As shown in Fig. S8,† the degradation ability of the composite photocatalyst was not significantly affected in real water samples, indicating the possibility of practical application. The water quality parameters of tap water and river water are listed in Table S3.†

Photocatalysis mechanism discussion

To explore the contribution of different active species to the degradation of chlortetracycline, the trapping experiments of active species were performed, in which $AgNO_3$ (an e^- scavenger), *p*-benzoquinone (BQ, a $^{\bullet}O_2^-$ scavenger), EDTA-2Na (an h^+ scavenger), and isopropanol (IPA, a $^{\bullet}OH$ scavenger) served as capturers for e^-, $^{\bullet}O_2^-$, h^+, and $^{\bullet}OH$, respectively.[45] As shown in Fig. 7a, the photocatalytic degradation performance of chlortetracycline was significantly decreased after adding $AgNO_3$, BQ, EDTA-2Na, and IPA to this solution, and the order of influence of these species on the photocatalytic degradation of chlortetracycline over **1**/GO/Fe_3O_4 was $^{\bullet}O_2^- > h^+ > e^- > {}^{\bullet}OH$. Therefore, it was demonstrated that e^-, $^{\bullet}O_2^-$, h^+, and $^{\bullet}OH$ all played key roles in chlortetracycline degradation. On this basis, electron spin resonance (ESR) technology was employed to further clarify the generation of $^{\bullet}OH$ and $^{\bullet}O_2^-$ in the reaction process of the photocatalytic system.[46,47] Dimethyl pyridine *N*-oxide (DMPO) in H_2O was used as a radical scavenger. As shown in Fig. 7b and c, no signals for $^{\bullet}OH$ and $^{\bullet}O_2^-$ were detected in the dark, while strong ESR signals can be observed after being irradiated for 10 minutes. Therefore, the existence of $^{\bullet}OH$ and $^{\bullet}O_2^-$ in chlortetracycline photodegradation is confirmed.

The photoluminescence emission is produced by the recombination of photoinduced electron–hole pairs, so photoluminescence analysis can be employed to prove the separation efficiency of the charge carriers in the composite.[48] As shown in Fig. 8a, **MOF-1** displayed strong photoluminescence emission when excited at 290 nm, while the emission intensity of **1**/GO/Fe_3O_4 decreased significantly, which confirmed a decreased recombination of the photogenerated carriers in **1**/GO/Fe_3O_4. Combined with the structural analysis of the composite, the interfacial contact between **MOF-1** and graphene oxide can enhance the separation of photogenerated electron–hole pairs and prolong the carrier lifetime, which would benefit the enhancement of the photocatalytic performance of **1**/GO/Fe_3O_4.

To further illustrate the effect of graphene oxide on photocatalytic performance, EIS measurements of **MOF-1** and **1**/GO/Fe_3O_4 were employed to study the process of charge transfer

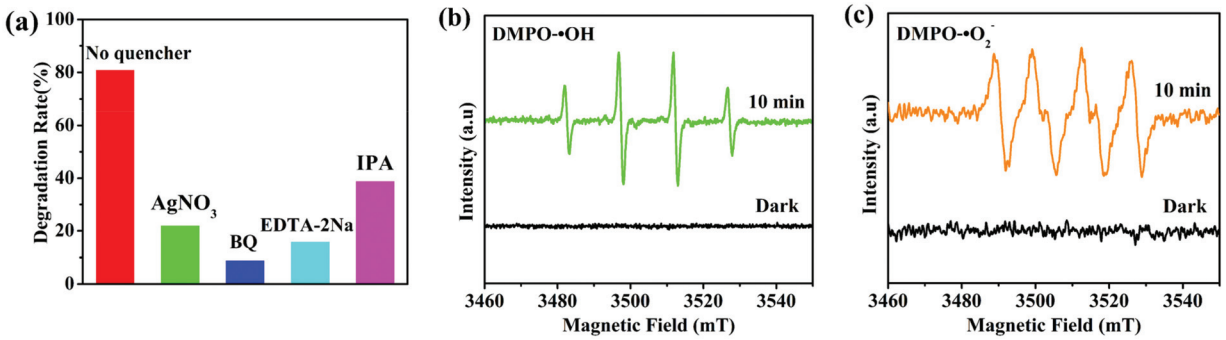

Fig. 7 (a) Effect of different scavengers on the photodegradation of chlortetracycline over **1**/GO/Fe_3O_4-9. ESR spectral investigation of the produced $^{\bullet}OH$ (b) and $^{\bullet}O_2^-$ (c) in the dark and after light radiation for 10 minutes (**1**/GO/Fe_3O_4 concentration: 0.45 g L^{-1}, H_2O_2 concentration: 10 mM, temperature: 25 °C).

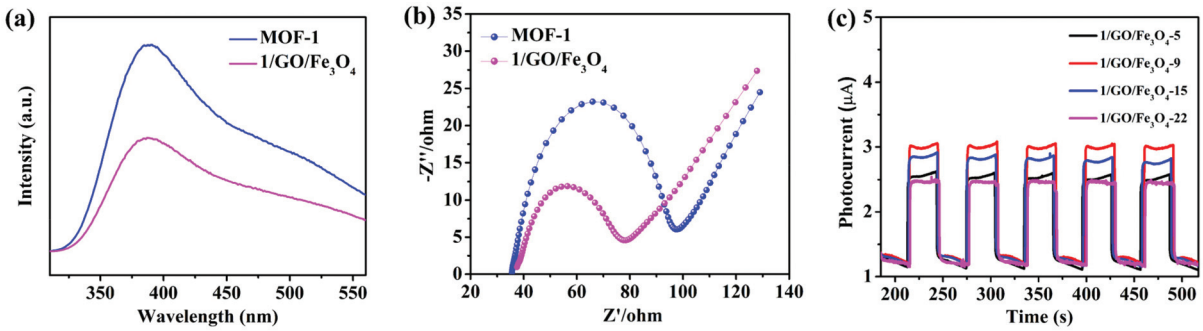

Fig. 8 (a) Photoluminescence spectra of **MOF-1** and **1**/GO/Fe_3O_4-9 (solid, temperature: 25 °C). (b) EIS Nyquist impedance plots of **MOF-1** and **1**/GO/Fe_3O_4-9. (c) Transient photocurrent responses of the **1**/GO/Fe_3O_4 composite.

and recombination.[49] As shown in Fig. 8b, **1**/GO/Fe_3O_4 showed a smaller radius of Nyquist arc than pure **MOF-1**, proving that an interfacial charge transferred to graphene oxide as the electron acceptor and led to the effective separation of photogenerated carriers in the photocatalytic reaction.[50] Similar results were obtained by other studies.[51–53] Besides, the EIS result was consistent with the photoluminescence analysis, proving that coating graphene oxide was an effective technique to improve the photocatalytic performance.

The enhanced charge transfer efficiency could also be evidenced by the experiment on transient photocurrent responses.[54] As presented in Fig. 8c, the photocurrent density of **1**/GO/Fe_3O_4-9 was superior to those of the other three composite samples, indicating the improved separation efficiency of photogenerated charge carriers in **1**/GO/Fe_3O_4-9.[55] This result was in agreement with the photocatalytic performance, confirming the optimum amount of graphene oxide in the composite. The photocurrent density of **MOF-1** was also tested, and the MOF itself had almost no photocurrent.

To examine the arrangement of energy levels, the electronic band structures of **MOF-1** and graphene oxide were examined by ultraviolet photoelectron spectroscopy. According to the data from ultraviolet photoelectron spectroscopy, the work function (Φ, the difference between the Fermi level and the vacuum level) and the valence band maximum (E_{VBM}) can be figured out. The E_{VBM} of **MOF-1** was located at 2.14 eV, below the Fermi level (E_{Fermi}), while Φ of **MOF-1** was quantified at 4.43 eV *versus* vacuum level (*vs.* vacuum) using the cutoff energy (Fig. S9a and S9b†).[48,56] The E_{Fermi} and E_{VBM} values in electron volts can be converted into electrochemical energy potentials in volts according to the reference standard in which 0 V *versus* normal hydrogen electrode (*vs.* NHE) equaled −4.44 eV *vs.* vacuum. Therefore, the E_{Fermi} and E_{VBM} of **MOF-1** were determined to be −0.01 V and 2.13 V (*vs.* NHE), respectively. Combined with the band-gap energies (Fig. S9c†) obtained from UV-Vis diffuse reflectance spectra and the empirical formula $E_{VB} = E_{CB} + E_g$, the conduction band minimum potential (E_{CBM}) of **MOF-1** was calculated to be −0.67 eV (*vs.* NHE). According to Fig. S10,† the Fermi position of graphene oxide was figured out to be 0.3 V (*vs.* NHE). The transfer of photogenerated electrons at the interface between semiconductors depended on their Fermi level. Owing to the coupling between Ce^{3+} cations and oxygen-containing functional groups of graphene oxide in the **1**/GO/Fe_3O_4 composite, **MOF-1** can be excited to yield photogenerated electron–hole pairs by visible light. Once **MOF-1** and graphene oxide were coupled, the photogenerated electrons in **MOF-1** can spontaneously transfer to the graphene oxide until their Fermi levels reached the dynamic equilibrium state (Fig. 9a). Thus, the **MOF-1** surface will accumulate positive charges and the graphene oxide surface will accumulate negative charges. Ultimately, an internal built-in electric field directed from **MOF-1** to graphene oxide at the interface was constructed, which helped to reduce the recombination of electrons and holes, thereby improving the photocatalytic performance.

To further confirm the results of ultraviolet photoelectron spectroscopy, Mott–Schottky tests were performed to obtain the flat-band potential (E_{FB}) of **MOF-1**. As shown in Fig. S9d,† the calculated E_{FB} of **MOF-1** was −0.65 eV (*vs.* NHE). For n-type semiconductors, the E_{CB} of the semiconductor was more negative (~0.1 eV) than the E_{FB}.[57] Therefore, the E_{CB} of **MOF-1** was about −0.75 eV. It is worth noting that the E_{CB} of **MOF-1** measured by Mott–Schottky plots was in good agreement with the E_{CBM} derived from ultraviolet photoelectron spectroscopy.[39] Given the more negative E_{CBM} of **MOF-1** in comparison to the reduction potential of $O_2/{}^{\bullet}O_2^-$, it was theoretically feasible for ${}^{\bullet}O_2^-$ generation to occur (Fig. 9b). Since the E_{VBM} for **MOF-1** was smaller than the redox potential of ${}^{\bullet}OH/OH^-$ (2.38 eV *vs.* NHE), ${}^{\bullet}OH$ cannot be generated. However, it was reasonable to speculate that the reduction of H_2O_2 can produce ${}^{\bullet}OH$ by photogenerated electrons in the **1**/GO/Fe_3O_4-H_2O_2-Vis system ($H_2O_2 + e^- \rightarrow OH^- + {}^{\bullet}OH$).[58] This should be

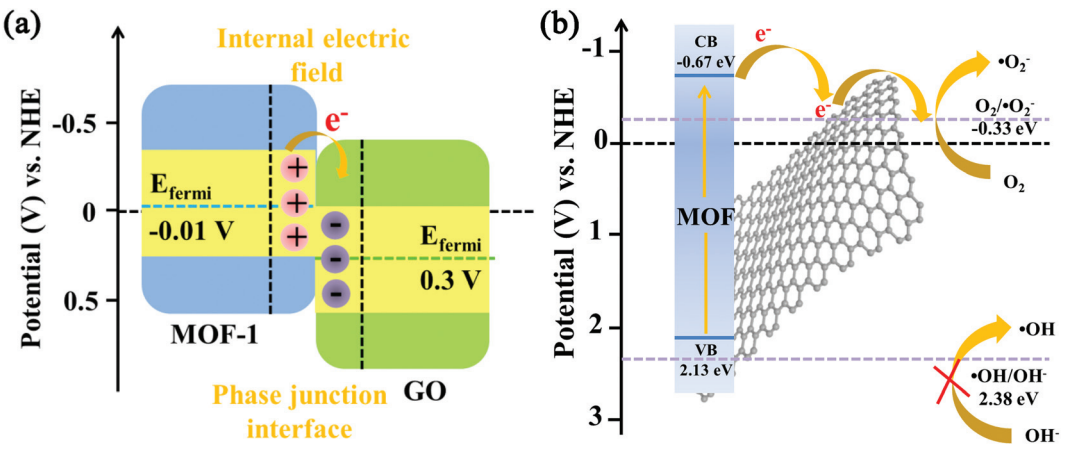

Fig. 9 (a) Energy band offset diagram and hetero-phase junction interface charge property. (b) Energy level diagram (*vs.* NHE) of the photocatalytic system.

the result of the synergistic effect in the H_2O_2-containing catalytic system. Similar to the trapping experiment results of active species, $^{\bullet}O_2^-$ and h^+ had more contribution than $^{\bullet}OH$ in photocatalytic performance.

Combined with the existing literature,[41,59] LC-MS was used to accurately detect and identify the possible photodegradation intermediates of chlortetracycline. As presented in Fig. S11a and b,† there was only one peak at m/z = 479.1 before the irradiation, which was identified as the molecular ion peak of chlortetracycline. After photocatalytic degradation, the initial concentration of chlortetracycline decreased at the retention time of 7.09 minutes, indicating the effective degradation of chlortetracycline (Fig. S11c†). The mass spectrum of the degradation of chlortetracycline illustrated in Fig. S11d and e† contains four transformation products, compounds I (m/z 510.88, R.T., 12.80 min), II (m/z 418.78, R.T., 12.77 min), III (m/z 316.95, R.T., 12.80 min), and IV (m/z 248.96, R.T., 12.80 min), respectively. Based on these intermediates, two possible degradation pathways of chlortetracycline are proposed in Scheme 1. By the ongoing degradation process, these intermediates may eventually be mineralized into CO_2, H_2O, Cl^-, *etc*.[10,60,61] The ICP data of the degraded solution showed that the content of iron ions in the solution was only 0.04%, which proved that Fe_3O_4 did not participate in the catalytic reaction.

Based on the above characterization studies and corresponding analyses, the boosting photocatalytic mechanism of **1**/GO/Fe_3O_4 was attributed to the synergistic effect of graphene oxide and Fe_3O_4 with **MOF-1**. Graphene oxide with substantial functional groups acted as a template for the growth of **MOF-1**, providing more reactive sites for photocatalysis, and served as an electron acceptor in the photocatalytic reaction, further extracting electrons from **MOF-1** and thus improving the photocatalytic performance. Furthermore, the presence of Fe_3O_4 surmounted the restriction that a powder photocatalyst was not easy to recover. Under visible light irradiation, **MOF-1** was excited and therefore generated photogenerated electrons (e^-) and holes (h^+). Meanwhile, **1**/GO/Fe_3O_4 can generate $^{\bullet}OH$ by catalyzing the decomposition of H_2O_2. Therefore, graphene oxide acts as an efficient electron capture trap in cooperation with MOFs to further extend the lifetime of photocarriers, which together with $^{\bullet}OH$ leads to effective chlortetracycline degradation.

$$\mathbf{1}/\mathrm{GO}/\mathrm{Fe_3O_4} + h\nu \rightarrow \mathbf{1}/\mathrm{GO}/\mathrm{Fe_3O_4}\ (e^- + h^+) \quad (1)$$

$$\mathbf{1}/\mathrm{GO}/\mathrm{Fe_3O_4}\ (e^-) + \mathrm{GO} \rightarrow \mathbf{1}/\mathrm{GO}/\mathrm{Fe_3O_4} + \mathrm{GO}\ (e^-) \quad (2)$$

$$\mathrm{GO}\ (e^-) + O_2 \rightarrow {}^{\bullet}O_2^- + \mathrm{GO} \quad (3)$$

$$H_2O_2 + e^- \rightarrow {}^{\bullet}OH + OH^- \quad (4)$$

$$^{\bullet}O_2^-(h^+/{}^{\bullet}OH) + \mathrm{CTC} \rightarrow \text{other products} \quad (5)$$

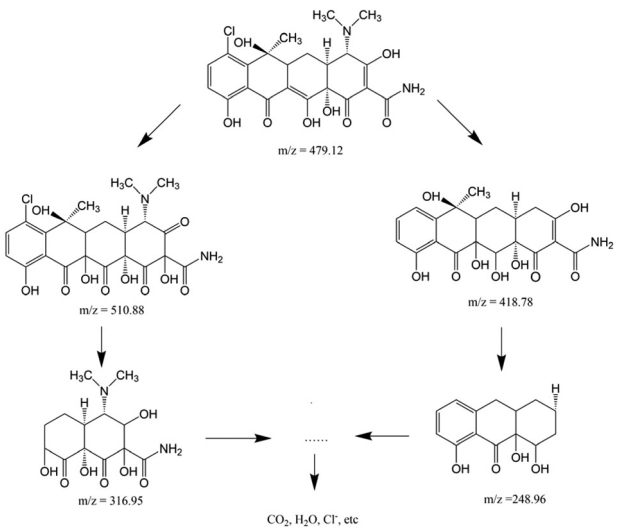

Scheme 1 Possible degradation pathway of chlortetracycline in the **1**/GO/Fe_3O_4 composite photocatalytic system.

Conclusion

In summary, a **1**/GO/Fe_3O_4 heterojunction has been successfully synthesized and proved to be an effective photocatalyst for the degradation of chlortetracycline. The introduction of graphene oxide broadened the light response range of the composite and greatly boosted the migration of photoexcited charge carriers due to the heterostructures between **MOF-1** and graphene oxide. The introduction of Fe_3O_4 helped the composite overcome the recycling restriction. Benefiting from the synergistic effect of graphene oxide and Fe_3O_4 on the **MOF-1**, **1**/GO/Fe_3O_4 eventually displayed enhanced photocatalytic activity. The boosting photocatalytic mechanism of **1**/GO/Fe_3O_4 photocatalysts was proposed by the charge transfer efficiency in the inner electric field produced by heterostructures between **MOF-1** and graphene oxide. Thus, graphene oxide as a carrier for electrons from **MOF-1** to graphene oxide effectively inhibited the recombination of photogenerated charge carriers. The findings of this work could pioneer a new path for the development of high-efficiency MOF/graphene-based material photocatalysts.

Conflicts of interest

There are no conflicts to declare.

Acknowledgements

This work was supported by the Natural Science Foundation of China (grant no. 21671124), the Fund for Shanxi "1331 Project" Key Innovative Research Team (1331KIRT), and the Undergraduate Research Training Plan Project of Shanxi University. A portion of this work was performed at the Scientific Instrument Center of Shanxi University of China. Partial support from the Robert A. Welch Foundation (B-0027) is also acknowledged (S. M.).

Notes and references

1 S. Sohrabnezhad, A. Pourahmad and M. F. Karimi, Magnetite-metal organic framework core@shell for degradation of ampicillin antibiotic in aqueous solution, *J. Solid State Chem.*, 2020, **288**, 121420.
2 H. Wang, X. Yuan, Y. Wu, G. Zeng, H. Dong, X. Chen, L. Leng, Z. Wu and L. Peng, In situ synthesis of In_2S_3@MIL-125(Ti) core–shell microparticle for the removal of tetracycline from wastewater by integrated adsorption and visible-light-driven photocatalysis, *Appl. Catal., B*, 2016, **186**, 19–29.
3 S. Fan, Y. Qu, L. Yao, J. Ren, R. Luque, Z. He and C. Bai, MOF-derived cluster-shaped magnetic nanocomposite with hierarchical pores as an efficient and regenerative adsorbent for chlortetracycline removal, *J. Colloid Interface Sci.*, 2021, **586**, 433–444.
4 H. B. Quesada, A. T. A. Baptista, L. F. Cusioli, D. Seibert, C. de Oliveira Bezerra and R. Bergamasco, Surface water pollution by pharmaceuticals and an alternative of removal by low-cost adsorbents: A review, *Chemosphere*, 2019, **222**, 766–780.
5 N. Barhoumi, H. Olvera-Vargas, N. Oturan, D. Huguenot, A. Gadri, S. Ammar, E. Brillas and M. A. Oturan, Kinetics of oxidative degradation/mineralization pathways of the antibiotic tetracycline by the novel heterogeneous electro-Fenton process with solid catalyst chalcopyrite, *Appl. Catal., B*, 2017, **209**, 637–647.
6 H. Fang, L. Han, Y. Cui, Y. Xue, L. Cai and Y. Yu, Changes in soil microbial community structure and function associated with degradation and resistance of carbendazim and chlortetracycline during repeated treatments, *Sci. Total Environ.*, 2016, **572**, 1203–1212.
7 B. Halling-Sørensen, A. Jacobsen, J. Jensen, G. SengeløV, E. Vaclavik and F. Ingerslev, Dissipation and effects of chlortetracycline and tylosin in two agricultural soils: A field–scale study in southern Denmark, *Environ. Toxicol. Chem.*, 2005, **24**, 802–810.
8 J. Tang, T. Shi, X. Wu, H. Cao, X. Li, R. Hua, F. Tang and Y. Yue, The occurrence and distribution of antibiotics in Lake Chaohu, China: Seasonal variation, potential source and risk assessment, *Chemosphere*, 2015, **122**, 154–161.
9 J. Zheng and L. Zhang, Rational design and fabrication of multifunctional catalyzer Co_2SnO_4-SnO_2/GC for catalysis applications: Photocatalytic degradation/catalytic reduction of organic pollutants, *Appl. Catal., B*, 2018, **231**, 34–42.
10 Y. Liu, Y. Gao, B. Yao and D. Zou, Removal of chlortetracycline by nano-micro-electrolysis materials: Application and mechanism, *Chemosphere*, 2020, **238**, 124543.
11 S. Liu, L. Mei, X. Liang, L. Liao, G. Lv, S. Ma, S. Lu, A. Abdelkader and K. Xi, Anchoring Fe_3O_4 Nanoparticles on Carbon Nanotubes for Microwave-Induced Catalytic Degradation of Antibiotics, *ACS Appl. Mater. Interfaces*, 2018, **10**, 29467–29475.
12 S. Lu, L. Liu, H. Demissie, G. An and D. Wang, Design and application of metal-organic frameworks and derivatives as heterogeneous Fenton-like catalysts for organic wastewater treatment: A review, *Environ. Int.*, 2021, **146**, 106273.
13 Y. Gao, J. Xia, D. Liu, R. Kang, G. Yu and S. Deng, Synthesis of mixed-linker Zr-MOFs for emerging contaminant adsorption and photodegradation under visible light, *Chem. Eng. J.*, 2019, **378**, 122118.
14 M. Zhang, L. Wang, T. Zeng, Q. Shang, H. Zhou, Z. Pan and Q. Cheng, Two pure MOF-photocatalysts readily prepared for the degradation of methylene blue dye under visible light, *Dalton Trans.*, 2018, **47**, 4251–4258.
15 S. Zhao, D. Chen, F. Wei, N. Chen, Z. Liang and Y. Luo, Removal of Congo red dye from aqueous solution with nickel-based metal-organic framework/graphene oxide composites prepared by ultrasonic wave-assisted ball milling, *Ultrason. Sonochem.*, 2017, **39**, 845–852.
16 W. Yi, C. Han, Z. Li, Y. Guo, M. Liu and C. Dong, A strategy of electrochemical simultaneous detection of acetaminophen and levofloxacin in water based on g-C_3N_4 nanosheet-doped graphene oxide, *Environ. Sci. Nano*, 2021, **8**, 258–268.
17 D. R. Dreyer, S. Park, C. W. Bielawski and R. S. Ruoff, The chemistry of graphene oxide, *Chem. Soc. Rev.*, 2010, **39**, 228–240.
18 M. Tanhaei, A. R. Mahjoub and V. Safarifard, Sonochemical synthesis of amide-functionalized metal-organic framework/graphene oxide nanocomposite for the adsorption of methylene blue from aqueous solution, *Ultrason. Sonochem.*, 2018, **41**, 189–195.
19 X. Sun, Q. Xia, Z. Zhao, Y. Li and Z. Li, Synthesis and adsorption performance of MIL-101(Cr)/graphite oxide composites with high capacities of n-hexane, *Chem. Eng. J.*, 2014, **239**, 226–232.
20 B. Peng, J. Cui, Y. Wang, J. Liu, H. Zheng, L. Jin, X. Zhang, Y. Zhang and Y. Wu, CeO_{2-x}/C/rGO nanocomposites derived from Ce-MOF and graphene oxide as a robust platform for highly sensitive uric acid detection, *Nanoscale*, 2018, **10**, 1939–1945.
21 B.-M. Jun, S. Sd. Elanchezhiyan, Y. Yoon, D. Wang, S. Kim, S. Muthu Prabhu and C. M. Park, Accelerated photocatalytic degradation of organic pollutants over carbonate-rich lanthanum-substituted zinc spinel ferrite assembled reduced graphene oxide by ultraviolet (UV)-activated persulfate, *Chem. Eng. J.*, 2020, **393**, 124733.
22 Z. Wang, J. Huang, J. Mao, Q. Guo, Z. Chen and Y. Lai, Metal–organic frameworks and their derivatives with graphene composites: preparation and applications in electrocatalysis and photocatalysis, *J. Mater. Chem. A*, 2020, **8**, 2934–2961.
23 Q.-Q. Zhu, H.-W. Zhang, R. Yuan and H. He, Ingenious fabrication of metal–organic framework/graphene oxide composites as aptasensors with superior electrochemical recognition capability, *J. Mater. Chem. C*, 2020, **8**, 15823–15829.
24 C. Yang, X. You, J. Cheng, H. Zheng and Y. Chen, A novel visible-light-driven In-based MOF/graphene oxide composite photocatalyst with enhanced photocatalytic activity

toward the degradation of amoxicillin, *Appl. Catal., B*, 2017, **200**, 673–680.

25 H. Fakhri and H. Bagheri, Highly efficient Zr-MOF@WO_3/graphene oxide photocatalyst: Synthesis, characterization and photodegradation of tetracycline and malathion, *Mater. Sci. Semicond. Process.*, 2020, **107**, 104815.

26 V. Jabbari, J. M. Veleta, M. Zarei-Chaleshtori, J. Gardea-Torresdey and D. Villagrán, Green synthesis of magnetic MOF@GO and MOF@CNT hybrid nanocomposites with high adsorption capacity towards organic pollutants, *Chem. Eng. J.*, 2016, **304**, 774–783.

27 M. Soleiman-Beigi and F. Mohammadi, A green and mild procedure to selective synthesis of diarylamine via domino reaction of aryl halides and arginine catalyzed by magnetic-MOF, *Heteroat. Chem.*, 2018, **29**, e21450.

28 C.-F. Zhang, L.-G. Qiu, F. Ke, Y.-J. Zhu, Y.-P. Yuan, G.-S. Xu and X. Jiang, A novel magnetic recyclable photocatalyst based on a core–shell metal–organic framework Fe_3O_4@MIL-100(Fe) for the decolorization of methylene blue dye, *J. Mater. Chem. A*, 2013, **1**, 14329–14334.

29 N. M. Mahmoodi, M. Oveisi and E. Asadi, Synthesis of NENU metal-organic framework-graphene oxide nanocomposites and their pollutant removal ability from water using ultrasound, *J. Cleaner Prod.*, 2019, **211**, 198–212.

30 J. Lin, H. Hu, N. Gao, J. Ye, Y. Chen and H. Ou, Fabrication of GO@MIL-101(Fe) for enhanced visible-light photocatalysis degradation of organophosphorus contaminant, *J. Water Process Eng.*, 2020, **33**, 101010.

31 S. Bao, H. Liang, C. Li and J. Bai, A heterostructure BiOCl nanosheets/TiO_2 hollow-tubes composite for visible light-driven efficient photodegradation antibiotic, *J. Photochem. Photobiol., A*, 2020, **397**, 112590.

32 Y. M. Hunge, A. A. Yadav, A. G. Dhodamani, N. Suzuki, C. Terashima, A. Fujishima and V. L. Mathe, Enhanced photocatalytic performance of ultrasound treated GO/TiO_2 composite for photocatalytic degradation of salicylic acid under sunlight illumination, *Ultrason. Sonochem.*, 2020, **61**, 104849.

33 J. Fonseca de Lima, F. V. S. Moreno, B. A. T. Menezes, J. S. Barbosa, M. C. Waddington, S. A. Franklin, G. J. Clarkson, M. Walker, O. A. Serra and R. I. Walton, Investigation of the preparation and reactivity of metal–organic frameworks of cerium and pyridine-2,4,6-tricarboxylate, *Dalton Trans.*, 2022, **51**, 145–155.

34 N. Liu, W. Huang, X. Zhang, L. Tang, L. Wang, Y. Wang and M. Wu, Ultrathin graphene oxide encapsulated in uniform MIL-88A(Fe) for enhanced visible light-driven photodegradation of RhB, *Appl. Catal., B*, 2018, **221**, 119–128.

35 Y. Li, L. Chen, Y. Wang and L. Zhu, Advanced nanostructured photocatalysts based on reduced graphene oxide-flower-like Bi_2WO_6 composites for an augmented simulated solar photoactivity activity, *Mater. Sci. Eng., B*, 2016, **210**, 29–36.

36 Q. Gong, Y. Liu and Z. Dang, Core-shell structured Fe_3O_4@GO@MIL-100(Fe) magnetic nanoparticles as heterogeneous photo-Fenton catalyst for 2,4-dichlorophenol degradation under visible light, *J. Hazard. Mater.*, 2019, **371**, 677–686.

37 M. Liu, D. Zou, T. Ma, Z. Liu and Y. Li, Simultaneous efficient adsorption and accelerated photocatalytic degradation of chlortetracycline hydrochloride over novel Fe-based MOGs under visible light irradiation assisted by hydrogen peroxide, *Inorg. Chem. Front.*, 2019, **6**, 1388–1397.

38 P. Wang and Q. Yuan, Photocatalytic degradation of tetracyclines in liquid digestate: Optimization, kinetics and correlation studies, *Chem. Eng. J.*, 2021, **410**, 128327.

39 M. Zhang, Q. Shi, X. Cheng, J. Yang, Z. Liu, T. Chen, Y. Qu, J. Wang, M. Xie and W. Han, Accelerated generation of hydroxyl radical through surface polarization on $BiVO_4$ microtubes for efficient chlortetracycline degradation, *Chem. Eng. J.*, 2020, **400**, 125871.

40 X. Yuan, H. Wang, Y. Wu, G. Zeng, X. Chen, L. Leng, Z. Wu and H. Li, One–pot self–assembly and photoreduction synthesis of silver nanoparticle–decorated reduced graphene oxide/MIL–125(Ti) photocatalyst with improved visible light photocatalytic activity, *Appl. Organomet. Chem.*, 2016, **30**, 289–296.

41 F. Guo, X. Huang, Z. Chen, L. Cao, X. Cheng, L. Chen and W. Shi, Construction of Cu_3P-$ZnSnO_3$-g-C_3N_4 p-n-n heterojunction with multiple built-in electric fields for effectively boosting visible-light photocatalytic degradation of broad-spectrum antibiotics, *Sep. Purif. Technol.*, 2021, **265**, 118477.

42 S. Liang, Y. Zhou, K. Kang, Y. Zhang, Z. Cai and J. Pan, Synthesis and characterization of porous TiO_2-NS/Pt/GO aerogel: A novel three-dimensional composite with enhanced visible-light photoactivity in degradation of chlortetracycline, *J. Photochem. Photobiol., A*, 2017, **346**, 1–9.

43 L. Nirumand, S. Farhadi, A. Zabardasti and A. Khataee, Synthesis and sonocatalytic performance of a ternary magnetic MIL-101(Cr)/RGO/$ZnFe_2O_4$nanocomposite for degradation of dye pollutants, *Ultrason. Sonochem.*, 2018, **42**, 647–658.

44 D.-D. Chen, X.-H. Yi, C. Zhao, H. Fu, P. Wang and C.-C. Wang, Polyaniline modified MIL-100(Fe) for enhanced photocatalytic Cr(VI) reduction and tetracycline degradation under white light, *Chemosphere*, 2020, **245**, 125659.

45 L. Zeng, J. Wang, Q. Qian, Q. Chen, X.-P. Liu, Y. Luo, H. Xue and Z. Li, Photocatalytic degradation of tetracycline hydrochloride over rugby-like β-Ga_2O_3 with a 3D hierarchically assembled porous structure for environmental remediation, *Catal. Sci. Technol.*, 2020, **10**, 3315–3323.

46 C.-C. Wang, X.-H. Yi and P. Wang, Powerful combination of MOFs and C_3N_4 for enhanced photocatalytic performance, *Appl. Catal., B*, 2019, **247**, 24–48.

47 K. Talukdar, B.-M. Jun, Y. Yoon, Y. Kim, A. Fayyaz and C. M. Park, Novel Z-scheme Ag_3PO_4/Fe_3O_4-activated biochar photocatalyst with enhanced visible-light catalytic perform-

ance toward degradation of bisphenol A, *J. Hazard. Mater.*, 2020, **398**, 123025.

48 Q. Mu, Y. Su, Z. Wei, H. Sun, Y. Lian, Y. Dong, P. Qi, Z. Deng and Y. Peng, Dissecting the interfaces of MOF-coated CdS on synergized charge transfer for enhanced photocatalytic CO_2 reduction, *J. Catal.*, 2021, **397**, 128–136.

49 L. K. B. Paragas, V. D. Dang, R. S. Sahu, S. Garcia-Segura, M. D. G. de Luna, J. A. I. Pimentel and R.-A. Doong, Enhanced visible-light-driven photocatalytic degradation of acetaminophen over CeO_2/I, K-codoped C_3N_4 heterojunction with tunable properties in simulated water matrix, *Sep. Purif. Technol.*, 2021, **272**, 117567.

50 K. Su, G.-X. Dong, W. Zhang, Z.-L. Liu, M. Zhang and T.-B. Lu, In Situ Coating $CsPbBr_3$ Nanocrystals with Graphdiyne to Boost the Activity and Stability of Photocatalytic CO_2 Reduction, *ACS Appl. Mater. Interfaces*, 2020, **12**, 50464–50471.

51 Q. Shi, Z. Li, L. Chen, X. Zhang, W. Han, M. Xie, J. Yang and L. Jing, Synthesis of SPR Au/$BiVO_4$ quantum dot/rutile-TiO_2 nanorod array composites as efficient visible-light photocatalysts to convert CO_2 and mechanism insight, *Appl. Catal., B*, 2019, **244**, 641–649.

52 J. Ke, X. Duan, S. Luo, H. Zhang, H. Sun, J. Liu, M. Tade and S. Wang, UV-assisted construction of 3D hierarchical rGO/Bi_2MoO_6 composites for enhanced photocatalytic water oxidation, *Chem. Eng. J.*, 2017, **313**, 1447–1453.

53 M. Xie, Q. Meng, P. Luan, Y. Feng and L. Jing, Synthesis of mesoporous TiO_2-coupled Fe_2O_3 as efficient visible nano-photocatalysts for degrading colorless pollutants, *RSC Adv.*, 2014, **4**, 52053–52059.

54 D. Ding, Z. Jiang, J. Jin, J. Li, D. Ji, Y. Zhang and L. Zan, Impregnation of semiconductor CdS NPs in MOFs cavities via double solvent method for effective photocatalytic CO_2 conversion, *J. Catal.*, 2019, **375**, 21–31.

55 L. Shi, T. Wang, H. Zhang, K. Chang, X. Meng, H. Liu and J. Ye, An Amine–Functionalized Iron(III) Metal–Organic Framework as Efficient Visible–Light Photocatalyst for Cr (VI) Reduction, *Adv. Sci.*, 2015, **2**, 1500006.

56 Q. Mu, W. Zhu, X. Li, C. Zhang, Y. Su, Y. Lian, P. Qi, Z. Deng, D. Zhang, S. Wang, X. Zhu and Y. Peng, Electrostatic charge transfer for boosting the photocatalytic CO_2 reduction on metal centers of 2D MOF/rGO hetero-structure, *Appl. Catal., B*, 2020, **262**, 118144.

57 X. Wang, X. Zhao, D. Zhang, G. Li and H. Li, Microwave irradiation induced UIO-66-NH_2 anchored on graphene with high activity for photocatalytic reduction of CO_2, *Appl. Catal., B*, 2018, **228**, 47–53.

58 Y. Liu, Y. Zhu, J. Xu, X. Bai, R. Zong and Y. Zhu, Degradation and mineralization mechanism of phenol by $BiPO_4$ photocatalysis assisted with H_2O_2, *Appl. Catal., B*, 2013, **142–143**, 561–567.

59 J. Zhao, Q. Song, Q. He, D. D. Dionysiou, F. Wu, Y. Feng and X. Zhang, Fabrication of $Bi_{1.81}MnNbO_{6.72}$/sulfite system for efficient degradation of chlortetracycline, *Chemosphere*, 2021, **268**, 129269.

60 X. Qiao, X. Liu, W. Zhang, Y. Cai, Z. Zhong, Y. Li and J. Lü, Superior photo-Fenton activity towards chlortetracycline degradation over novel g–$_3N_4$ nanosheets/schwertmannite nanocomposites with accelerated Fe(III)/Fe(II) cycling, *Sep. Purif. Technol.*, 2021, **279**, 119760.

61 J. Zheng, X. Liu and L. Zhang, Design of porous double-shell Cu_2O@$CuCo_2O_4$ Z-Scheme hollow microspheres with superior redox property for synergistic photocatalytic degradation of multi-pollutants, *Chem. Eng. J.*, 2020, **389**, 124339.